INTERNATIONAL JOURNAL FOR NUMERICAL METHODS IN ENGINEERING
Int. J. Numer. Meth. Engng 2006; **65**:1243–1268
Published online 23 September 2005 in Wiley InterScience (www.interscience.wiley.com). DOI: 10.1002/nme.1487

Inverse geometry heat transfer problem based on a radial basis functions geometry representation

Marcial Gonzalez and Marcela B. Goldschmit*, †

Center for Industrial Research, FUDETEC, Dr. Jorge A. Simini 250, B2804MHA, Campana, Buenos Aires, Argentina

SUMMARY

We present a methodology for solving a non-linear inverse geometry heat transfer problem where the observations are temperature measurements at points inside the object and the unknown is the geometry of the volume where the problem is defined. The representation of the geometry is based on radial basis functions (RBFs) and the non-linear inverse problem is solved using the iteratively regularized Gauss–Newton method. In our work, we consider not only the problem with no geometry restrictions but also the bound-constrained problem.

The methodology is used for the industrial application of estimating the location of the 1150°C isotherm in a blast furnace hearth, based on measurements of the thermocouples located inside it. We validate the solution of the algorithm against simulated measurements with different levels of noise and study its behaviour on different regularization matrices. Finally, we analyse the error behaviour of the solution. Copyright © 2005 John Wiley & Sons, Ltd.

KEY WORDS: heat conduction; inverse geometry problem; radial basis functions; iteratively regularized Gauss–Newton method; blast furnace hearth

1. INTRODUCTION

Inverse heat transfer problems are important for various industrial applications. The purpose of inverse heat transfer problems is to recover causal characteristics from information about the temperature field. Causal characteristics of heat transfer are boundary conditions and their parameters, initial conditions, thermophysical properties, volumetric heat sources as well as geometric characteristics of the studied object.

In this paper, we present a methodology for solving a non-linear *inverse geometry heat transfer problem* where the observations are temperature measurements at points inside the

*Correspondence to: Marcela B. Goldschmit, Center for Industrial Research, FUDETEC, Dr. Jorge A. Simini 250, B2804MHA, Campana, Buenos Aires, Argentina.
†E-mail: sidgld@siderca.com

Contract/grant sponsor: SIDERAR

Received 3 January 2005
Revised 18 March 2005
Accepted 20 July 2005

Copyright © 2005 John Wiley & Sons, Ltd.

object and the unknown is the geometry of the volume where the problem is defined. In Section 2, we formally define the general inverse heat transfer problem and describe the finite element model developed to solve the direct heat transfer problem.

There are a number of publications dealing with industrial applications of inverse geometry problems (IGPs). Wawrzynek *et al.* [1] have combined IGPs with infrared tomography in order to study non-destructive evaluation of surface damages in concrete structural elements. Park *et al.* [2] have developed a model to identify the boundary shape of a domain dominated by natural convection, which can be potentially applied in the determination of a phase change isotherm in the Bridgman crystal growth of semiconductor materials. Kwag *et al.* [3] have estimated the phase front motion of ice by applying an IGP; this model has been used by the authors for controlling and monitoring a latent heat energy storage system. Huang *et al.* [4] have proposed to use an IGP to estimate the shape of frost growth on an evaporating tube by using temperature readings. Ganapathysubramanian *et al.* [5] have presented a framework to evaluate the shape sensitivity of finite thermo-inelastic deformations and have applied the method to the design of open- and closed-die forging processes.

It is well-known that inverse problems are typically ill-posed in the sense that small observation perturbations can lead to big errors in the solution. Such problems do not fulfill Hadamard's postulates of well-posedness [6, 7], where one of the following properties does not hold: a solution exists for all admissible data, the solution is unique, the solution depends continuously on the data. Therefore, regularization methods have to be applied in order to guarantee a stable solution.

Several regularization methods have been used in the literature to handle non-linear ill-posed problems [6, 7] by replacing the original ill-posed problem with a well-posed approximated problem. Iterative regularization appears to be one of the most efficient approaches for the construction of stable algorithms for solving non-linear inverse problems [7]. Among this type of methods, we use the iteratively regularized Gauss–Newton method [8–13]. In Section 3, we formulate the inverse geometry problem considering the case of a linear combination of several regularization matrices and a bound constrained problem with geometry restrictions.

In this work, the estimated geometry of the object is described by polyharmonic radial basis functions (RBFs) from a set of interpolation points defined by a set of parameters which are actually the inverse geometry problem unknowns. RBFs are used both because they impose few restrictions on the geometry of the interpolation points which do not need to lie on a regular grid, and because they provide a smooth interpolation [14–19].

Radial basis functions are a recent tool for interpolating data and have been used in many areas. Perrin *et al.* [16] and Carr *et al.* [15] have used RBFs in medical imaging; Turk *et al.* [20] and Carr *et al.* [14] have modelled surfaces implicitly with RBFs in computer graphics; Kansa [18, 19] has introduced the RBFs method for solving partial differential equations; and Belytschko *et al.* [21] have developed a structured finite element method for solids which uses RBFs to implicitly define surfaces. Frankle [17] has found that the RBFs are the best 2D scheme among 29 different methods for scattered data interpolation.

In Section 4, we present the parameterization of the geometry, an introduction to RBFs interpolation and a description of a simple bidimensional remeshing algorithm developed by us.

The industrial problem to be solved in this paper is the estimation of the blast furnace hearth wear. One of the most critical parts of the blast furnace is its hearth, which cannot be repaired or relined without interrupting its production for a long time. Therefore, the blast furnace

Copyright © 2005 John Wiley & Sons, Ltd.

campaign is mainly limited by the hearth refractory wear which is produced by thermo-chemical solution and thermo-mechanical damage [22]. Since direct measurements of the remaining lining thickness are impossible to be obtained, we use information about the thermal state of the blast furnace hearth to estimate the erosion profile. Moreover, the location of the 1150°C isotherm is particularly useful because it represents a potential limit on the penetration of liquid iron into the hearth wall porosity (1150°C is the eutectic temperature of carbon saturated iron [22]).

In Section 5, we develop the industrial application of estimating the location of the 1150°C isotherm in a blast furnace hearth, based on measurements of thermocouples located inside it [23–26]. Further, we validate the solution of the algorithm against simulated measurements with different levels of noise and study its behaviour on different regularization matrices. We analyse the problem with no geometry restrictions but also the bound-constrained problem. Finally, we study the error behaviour of the solution.

The last section deals with the work conclusions.

2. DEFINITION OF THE GENERAL PROBLEM

Consider a general steady-state heat transfer problem defined on an arbitrary volume (Ω) which has a fixed boundary ($\partial\Omega_n$) where natural boundary conditions are applied, and an unknown boundary ($\partial\Omega_T$) where a known temperature is applied. The shape and number of materials that the volume Ω contains will depend on the location of the boundary $\partial\Omega_T$. As shown in Figures 1(a) and (b), since the materials are on fixed positions, different locations of the boundary $\partial\Omega_T$ cause different shapes of materials M3 and M4.

Our purpose is to determine the location of the boundary $\partial\Omega_T$, and so the geometry of the volume Ω, matching a set of temperatures measured at certain points located inside the volume. Therefore, our general problem is an inverse geometry heat transfer problem where the observations are temperature measurements at points inside the volume and the unknown is the geometry of the volume where the problem is defined.

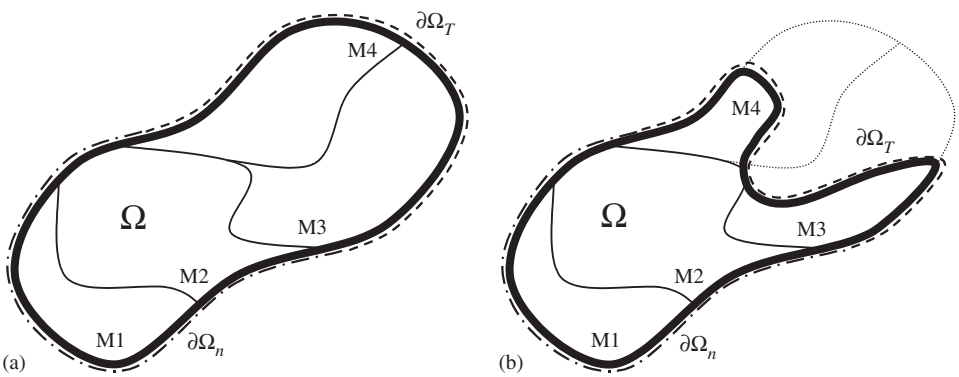

Figure 1. Schematic of the general problem.

Copyright © 2005 John Wiley & Sons, Ltd.

2.1. The direct heat transfer problem

The direct problem solution is a prerequisite for the solution of the inverse problem. Our direct problem is a steady-state heat transfer problem governed by

$$\nabla \cdot (k \nabla T) = 0 \quad \forall \mathbf{x} \in \Omega \tag{1}$$

where k is the temperature-dependent thermal conductivity, $\Omega \subset \mathbb{R}^{n_{\text{dim}}}$ is a bounded domain with $1 \leqslant n_{\text{dim}} \leqslant 3$, and $\partial\Omega$ is the smooth boundary of Ω.

Equation (1) is subjected to the following boundary conditions on $\partial\Omega_T$, $\partial\Omega_q$ and $\partial\Omega_c$, complementary parts of $\partial\Omega$ ($\partial\Omega_n = \partial\Omega_q \cup \partial\Omega_c$, $\partial\Omega_q \cap \partial\Omega_c = \emptyset$ and $\partial\Omega = \partial\Omega_T \cup \partial\Omega_n$, $\partial\Omega_T \cap \partial\Omega_n = \emptyset$):

- Dirichlet boundary condition on $\partial\Omega_T$:

$$T = T_w \quad \forall \mathbf{x} \in \partial\Omega_T \tag{2}$$

  where T_w is a given imposed temperature.
- Neumann boundary condition on $\partial\Omega_q$:

$$-k \nabla T \cdot \mathbf{n} = q_w \quad \forall \mathbf{x} \in \partial\Omega_q \tag{3}$$

  where q_w is a given normal heat flux and $\mathbf{n}$ is the outward normal to the surface $\partial\Omega$.
- Robin boundary condition on $\partial\Omega_c$:

$$-k \nabla T \cdot \mathbf{n} = h(T - T_\infty) \quad \forall \mathbf{x} \in \partial\Omega_c \tag{4}$$

  where h is the convective heat transfer coefficient and T_∞ is the ambient temperature.

The Galerkin finite element method [27, 28] is used to solve the direct heat transfer problem. Thus, we obtain the following system of equations:

$$(\mathbf{K}^k + \mathbf{K}^c)\mathbf{T}^{\text{FEM}} - \mathbf{F} = \mathbf{0} \tag{5}$$

where $\mathbf{T}^{\text{FEM}}$ is the vector of nodal temperatures, $\mathbf{K}^k$ is the conductivity matrix, $\mathbf{K}^c$ is the thermal convection matrix and $\mathbf{F}$ is the thermal load vector, given by

$$\tilde{T} = \mathbf{N}\mathbf{T}^{\text{FEM}} \tag{6}$$

$$\mathbf{K}^k = \int_\Omega \mathbf{B}^{\text{T}} \mathbf{k} \mathbf{B} \, \mathrm{d}V \tag{7}$$

$$\mathbf{K}^c = \int_{\partial\Omega_c} h \mathbf{N}^{\text{T}} \mathbf{N} \, \mathrm{d}S \tag{8}$$

$$\mathbf{F} = \int_{\partial\Omega_c} h \mathbf{N}^{\text{T}} T_\infty \, \mathrm{d}S - \int_{\partial\Omega_q} \mathbf{N}^{\text{T}} q_w \, \mathrm{d}S \tag{9}$$

where $\tilde{T}$ is the approximated temperature field, $\mathbf{N}$ is the finite element interpolation matrix, and $\mathbf{B}$ is the temperature-gradient interpolation matrix whose components are $B_{ij} = \partial N_j / \partial x_i$.

The equations are non-linear because the thermal conductivity is temperature-dependent; therefore, it is necessary to solve them using an iterative technique.

Copyright © 2005 John Wiley & Sons, Ltd.

3. FORMULATION OF THE INVERSE GEOMETRY PROBLEM

We consider our problem in finite-dimensional subspaces because we aim at obtaining practical applications. This means that not only the number of measurements is finite, but also the location of the unknown boundary $\partial\Omega_T$ is parameterized in order to obtain the approximate solution numerically.

Therefore, we parameterize the location of the unknown boundary $\partial\Omega_T$ by a set of n_p parameters $\mathbf{p} = (p_1, \ldots, p_{n_p})$, and we formulate the inverse problem as finding the geometry parameters $\mathbf{p}^*$ such that

$$\mathbf{p}^* = \arg \min_{\mathbf{p} \in \mathbb{R}^{n_p}} \mathscr{F}_{(\mathbf{p})} \tag{10}$$

where $\mathscr{F}_{(\mathbf{p})}$ is a function defined by the least-square error between the calculated and measured temperatures. Thus, $\mathscr{F}_{(\mathbf{p})}$ is given by

$$\mathscr{F}_{(\mathbf{p})} = \frac{1}{2}\|\mathbf{T}_{(\mathbf{p})} - \mathbf{T}^{\mathrm{Obs}}\|^2 = \frac{1}{2}\sum_{i=1}^{n_{\mathrm{obs}}} [\tilde{T}_{(\mathbf{x}_i^{\mathrm{Obs}}, \mathbf{p})} - T_i^{\mathrm{Obs}}]^2 \tag{11}$$

where T_i^{Obs} is the temperature measured at point $\mathbf{x}_i^{\mathrm{Obs}}$, $\tilde{T}_{(\mathbf{x}_i^{\mathrm{Obs}}, \mathbf{p})}$ is the temperature calculated by the finite element model using the geometry parameters $\mathbf{p}$, and n_{obs} is the number of observations.

It is well-known that inverse problems are typically ill-posed in the sense that small observation perturbations can lead to big errors in the solution [6, 7]. Therefore, it is necessary to apply regularization methods in order to guarantee a stable solution. Several regularization methods have been used in the literature, and iterative regularization appears to be one of the most efficient approaches for the construction of stable algorithms for solving non-linear inverse problems [7]. Among this type of methods, we use the iteratively regularized Gauss–Newton method.

3.1. Iteratively regularized Gauss–Newton method

We use a discrete scheme of the iteratively regularized Gauss–Newton method [8–13], whose iterative solution is defined by

$$\begin{aligned} {}^{\mathrm{GN}}\mathbf{p}^{\mathrm{Iter}+1} = \mathbf{p}^{\mathrm{Iter}} &+ [\mathbf{DT}^{\mathrm{T}}_{(\mathbf{p}^{\mathrm{Iter}})}\mathbf{DT}_{(\mathbf{p}^{\mathrm{Iter}})} + \alpha_{\mathrm{Iter}}\mathbf{L}^{\mathrm{T}}\mathbf{L}]^{-1} \\ &\cdot[\mathbf{DT}^{\mathrm{T}}_{(\mathbf{p}^{\mathrm{Iter}})}\boldsymbol{\Delta}\mathbf{T}^{\mathrm{Obs}}_{(\mathbf{p}^{\mathrm{Iter}})} + \alpha_{\mathrm{Iter}}\mathbf{L}^{\mathrm{T}}\mathbf{L}(\mathbf{p}^{\triangle} - \mathbf{p}^{\mathrm{Iter}})] \end{aligned} \tag{12}$$

where Iter denotes the iteration number; $\mathbf{DT}_{(\mathbf{p})}$ is the sensitivity matrix; $\mathbf{L}$ is some regularization matrix; $\boldsymbol{\Delta}\mathbf{T}^{\mathrm{Obs}}_{(\mathbf{p})}$ is a vector whose components are $[T_i^{\mathrm{Obs}} - \tilde{T}_{(\mathbf{x}_i^{\mathrm{Obs}}, \mathbf{p})}]$ with $i = 1, n_{\mathrm{obs}}$; $\mathbf{p}^{\triangle}$ is an *a priori* suitable approximation of the unknown set of parameters; and $\alpha_{\mathrm{Iter}} > 0$ is the regularization parameter.

Further, the solution calculated with the iteratively regularized Gauss–Newton method, ${}^{\mathrm{GN}}\mathbf{p}^{\mathrm{Iter}+1}$, is used to update $\mathbf{p}^{\mathrm{Iter}}$ as follows:

$$\mathbf{p}^{\mathrm{Iter}+1} = \mathbf{p}^{\mathrm{Iter}} + \beta^{\mathrm{Iter}}({}^{\mathrm{GN}}\mathbf{p}^{\mathrm{Iter}+1} - \mathbf{p}^{\mathrm{Iter}}) \tag{13}$$

Copyright © 2005 John Wiley & Sons, Ltd.

where $\beta^{\text{Iter}}>0$ is a step length such that

$$\mathscr{F}^*_{(\mathbf{p}^{\text{Iter}+1})}<\mathscr{F}^*_{(\mathbf{p}^{\text{Iter}})} \tag{14}$$

with

$$\mathscr{F}^*_{(\mathbf{p})}=\tfrac{1}{2}\|\mathbf{T}_{(\mathbf{p})}-\mathbf{T}^{\text{Obs}}\|^2+\tfrac{1}{2}\alpha\|\mathbf{L}(\mathbf{p}-\mathbf{p}^{\triangle})\|^2 \tag{15}$$

The selection of a step length makes sense due to the highly non-linear nature of the function $\mathscr{F}^*_{(\mathbf{p})}$, in which case β^{Iter} is typically less than 1.00.

3.1.1. Evaluation of the sensitivity matrix. The sensitivity matrix components are the partial derivatives of the temperature with respect to the set of geometry parameters. We evaluate them using a 'discretize-then-differenciate' approach [29], which means that we first discretize the temperature field and then we differentiate it by a finite difference approximation

$$\left.\frac{\partial T}{\partial p_j}\right|_{(\mathbf{x},\,\mathbf{p})}\approx\frac{\tilde{T}_{(\mathbf{x},\,\{p_1,\ldots,p_j+\Delta p_j,\ldots,p_{n_p}\})}-\tilde{T}_{(\mathbf{x},\,\{p_1,\ldots,p_j,\ldots,p_{n_p}\})}}{\Delta p_j} \tag{16}$$

Therefore, the sensitivity matrix can be written as

$$\mathbf{DT}_{(\mathbf{p})}=\begin{bmatrix}\mathbf{N}_{(\mathbf{x}_1^{\text{Obs}})}\left.\dfrac{\partial\mathbf{T}}{\partial p_1}\right|^{\text{FEM}}_{(\mathbf{p})} & \cdots & \mathbf{N}_{(\mathbf{x}_1^{\text{Obs}})}\left.\dfrac{\partial\mathbf{T}}{\partial p_{n_p}}\right|^{\text{FEM}}_{(\mathbf{p})}\\ \vdots & \ddots & \vdots\\ \mathbf{N}_{(\mathbf{x}_{n_{\text{obs}}}^{\text{Obs}})}\left.\dfrac{\partial\mathbf{T}}{\partial p_1}\right|^{\text{FEM}}_{(\mathbf{p})} & \cdots & \mathbf{N}_{(\mathbf{x}_{n_{\text{obs}}}^{\text{Obs}})}\left.\dfrac{\partial\mathbf{T}}{\partial p_{n_p}}\right|^{\text{FEM}}_{(\mathbf{p})}\end{bmatrix}\in\mathbb{R}^{n_{\text{obs}}\times n_p} \tag{17}$$

where $\left.\frac{\partial\mathbf{T}}{\partial p_j}\right|^{\text{FEM}}_{(\mathbf{p})}$ are vectors of nodal sensitivities with respect to the parameter p_j, such that

$$\left.\frac{\partial T}{\partial p_j}\right|_{(\mathbf{x},\,\mathbf{p})}\approx\mathbf{N}_{(\mathbf{x})}\left.\frac{\partial\mathbf{T}}{\partial p_j}\right|^{\text{FEM}}_{(\mathbf{p})} \tag{18}$$

The components of these nodal sensitivity vectors can be easily obtained from definition (16) because the finite element discretization support is the same as the one we use for the temperature field.

3.1.2. Evaluation of the regularization matrix. The regularization matrix $\mathbf{L}$ is the discrete form of some differential operators [13, 30]. We choose a combination of the identity matrix $\mathbf{I}$ and discrete approximations of derivative operators given by

$$\mathbf{L}^{\text{T}}\mathbf{L}=\sum_{k=0}^{2}w_k\mathbf{L}_k^{\text{T}}\mathbf{L}_k \tag{19}$$

Copyright © 2005 John Wiley & Sons, Ltd.

where

$$\mathbf{L}_0 = \mathbf{I} \in \mathbb{R}^{n_p \times n_p} \tag{20}$$

$$\mathbf{L}_1 = \begin{bmatrix} 1 & -1 & & \\ & \ddots & \ddots & \\ & & 1 & -1 \end{bmatrix} \in \mathbb{R}^{(n_p-1)\times n_p} \tag{21}$$

$$\mathbf{L}_2 = \begin{bmatrix} 1 & 2 & -1 & & \\ & \ddots & \ddots & \ddots & \\ & & 1 & 2 & -1 \end{bmatrix} \in \mathbb{R}^{(n_p-2)\times n_p} \tag{22}$$

and $w_k \geqslant 0$ are weighting factors such that $\sum_{k=0}^{2} w_k = 1$. In Section 5, we analyse the solution behaviour on different regularization matrices.

3.1.3. Determination of the regularization parameter. The regularization parameter $\alpha_{\text{Iter}} > 0$ is *a priori* chosen such that

$$1 \geqslant \frac{\alpha_{\text{Iter}+1}}{\alpha_{\text{Iter}}} \geqslant r, \qquad \lim_{\text{Iter}\to\infty} \alpha_{\text{Iter}} = 0 \tag{23}$$

with $r < 1$. This monotically decreasing sequence has as its first term the optimal regularization parameter for the Tikhonov regularization method [6]

$$\alpha_0 \sim \delta^{2/2\nu+1}, \qquad \nu \in [1/2;\, 1] \tag{24}$$

where δ is called the noise level.

3.1.4. Convergence criterion. Due to the instability of ill-posed problems, the iteration must not be arbitrarily continued when iterative regularization methods are used. Instead, the iterative process must be stopped at the right iteration because only for an appropriate stopping iteration, a stable solution is yielded. As shown in Figure 2, while the observation function (Equation (11)) decreases as the number of iterations increases, the error in the parameters (assuming the real solution known) starts to increase after certain number of iterations. Therefore, a stopping rule must be properly chosen.

We use the discrepancy principle as a stopping rule [6, 10–13], that is, the iterative process is repeated until the iteration Iter_δ, such that

$$\|\mathbf{T}_{(\mathbf{p}^{\text{Iter}_\delta})} - \mathbf{T}^{\text{Obs}}\| \leqslant \tau\delta < \|\mathbf{T}_{(\mathbf{p}^{\text{Iter}})} - \mathbf{T}^{\text{Obs}}\| \quad 0 \leqslant \text{Iter} < \text{Iter}_\delta \tag{25}$$

for some $\tau > 1$.

The discrepancy principle is based on stopping as soon as the observation function is in the order of the noise level, which means that the best approximation one should expect is in the order of the data error.

Copyright © 2005 John Wiley & Sons, Ltd.

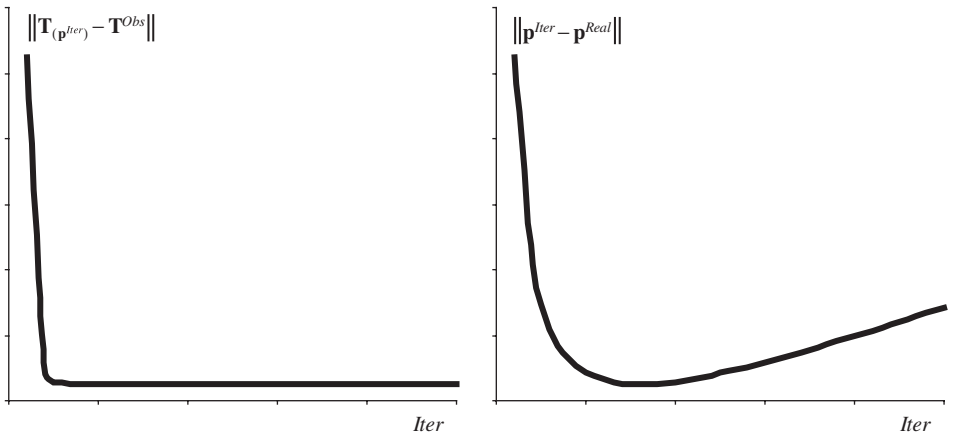

Figure 2. Typical error behaviour.

3.2. The bound-constrained problem

We stated our inverse geometry problem as finding the location of the boundary $\partial\Omega_T$, which is parameterized by a set of parameters $\mathbf{p}$, such that a set of temperature measurements at points inside the volume is matched. But the location of the boundary $\partial\Omega_T$ may be subjected to some geometry restrictions, typically the thermally unloaded geometry bounds. These geometry restrictions can be expressed as geometry parameters bounds depending on the parameterization adopted.

Consequently, as Equation (12) has the following variational form:

$$\mathscr{F}_{(\mathbf{p})}^{\text{Iter}} = \tfrac{1}{2}\|\mathbf{DT}_{(\mathbf{p}^{\text{Iter}})}(\mathbf{p} - \mathbf{p}^{\text{Iter}}) - \mathbf{\Delta T}_{(\mathbf{p}^{\text{Iter}})}^{\text{Obs}}\|^2 + \tfrac{1}{2}\alpha\|\mathbf{L}(\mathbf{p} - \mathbf{p}^{\Delta})\|^2 \tag{26}$$

we reduce the original problem to a bound-constrained problem

$$\begin{aligned} &\min_{\mathbf{p}\in\mathbb{R}^{n_p}} \quad \mathscr{F}_{(\mathbf{p})}^{\text{Iter}} \\ &\text{subject to} \quad g_{(\mathbf{p})}^{k} \leqslant 0 \quad k = 1, n_p \end{aligned} \tag{27}$$

where $g_{(\mathbf{p})}^{k} = p_k - p_k^{\max}$ are the geometry parameters inequality constraint conditions.

The Lagrange multiplier method [31] is used to convert the constraint minimization problem into a simpler problem, such that

$$\mathbf{p}^{\text{Iter}+1} = \arg \min_{\mathbf{p}\in\mathbb{R}^{n_p}} (\mathscr{F}_{(\mathbf{p})}^{\text{Iter}} + \lambda_k g_{(\mathbf{p})}^{k}) \tag{28}$$

where λ_k are the Lagrange multipliers.

Copyright © 2005 John Wiley & Sons, Ltd.

Therefore, the discrete scheme of the iteratively regularized Gauss–Newton method (12) is replaced by the bound-constrained problem iterative solution

$$\begin{bmatrix} \mathbf{DT}^{\mathrm{T}}_{(\mathbf{p}^{\mathrm{Iter}})}\mathbf{DT}_{(\mathbf{p}^{\mathrm{Iter}})} + \alpha\mathbf{L}^{\mathrm{T}}\mathbf{L} & \mathbf{DG}^{\mathrm{T}}_{({}^{r}\mathbf{p})} \\ \mathbf{DG}_{({}^{r}\mathbf{p})} & \mathbf{0} \end{bmatrix} \cdot \begin{bmatrix} \delta\mathbf{p} \\ \delta\boldsymbol{\lambda} \end{bmatrix} = \begin{bmatrix} \mathbf{DT}^{\mathrm{T}}_{(\mathbf{p}^{\mathrm{Iter}})}\boldsymbol{\Delta}\mathbf{T}^{\mathrm{Obs}}_{(\mathbf{p}^{\mathrm{Iter}})} + \alpha\mathbf{L}^{\mathrm{T}}\mathbf{L}(\mathbf{p}^{\Delta} - \mathbf{p}^{\mathrm{Iter}}) - \mathbf{DG}^{\mathrm{T}}_{({}^{r}\mathbf{p})}{}^{r}\boldsymbol{\lambda} \\ -\mathbf{G}_{({}^{r}\mathbf{p})} \end{bmatrix} \tag{29}$$

where

$$\mathbf{DG}_{(\mathbf{p})} = \left.\frac{\partial g^{k}}{\partial p_{j}}\right|_{(\mathbf{p})} \in \mathbb{R}^{n_{\mathrm{ac}} \times n_{p}}, \quad \forall g^{k}_{(\mathbf{p})} > 0 \tag{30}$$

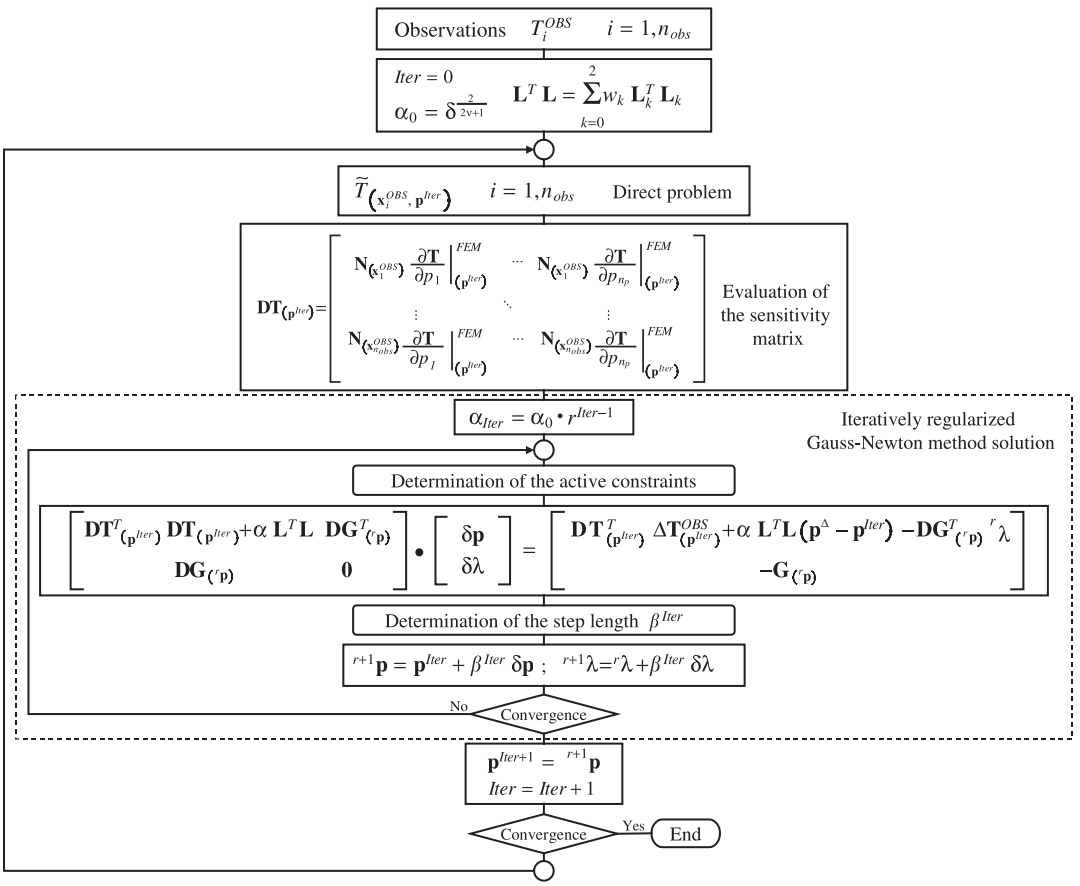

Figure 3. Iterative algorithm of the non-linear inverse problem.

Copyright © 2005 John Wiley & Sons, Ltd.

r indicates the iteration of the optimization subproblem, and n_{ac} is the number of active constraints. Note that the dimension of the equation system to be solved changes as the number of active constraints changes.

The solution is iteratively updated as follows:

$$^{r+1}\mathbf{p} = \mathbf{p}^{\text{Iter}} + \beta^{\text{Iter}}\delta\mathbf{p} \tag{31}$$

$$^{r+1}\boldsymbol{\lambda} = {}^{r}\boldsymbol{\lambda} + \beta^{\text{Iter}}\delta\boldsymbol{\lambda} \tag{32}$$

until a convergence criterion is satisfied. As a result, we obtain an acceptable feasible solution of $\mathbf{p}^{\text{Iter}+1}$ from this optimization subproblem.

3.3. The algorithm

In Figure 3, we show the iterative algorithm of the non-linear inverse problem. There are three different steps involved in the iterative process:

- the solution of the direct problem,
- the evaluation of the sensitivity matrix, which requires to solve the direct problem several times, and
- the determination of the iteratively regularized Gauss–Newton method solution of the bound-constrained problem, which also requires to solve the direct problem several times when the optimal step length is determined.

4. PARAMETERIZATION OF THE GEOMETRY

As stated in Section 3, the location of the unknown boundary $\partial\Omega_T$ is parameterized by $\mathbf{p} = (p_1, \ldots, p_{n_p})$, a set of n_p parameters. In addition, each parameter p_i has a base point with co-ordinates $\mathbf{BP}_{p_i}$ and a direction vector $\mathbf{DV}_{p_i}$; therefore, the definition of the unknown boundary is given by

$$\mathbf{SP}_{p_i} = \mathbf{BP}_{p_i} + p_i\mathbf{DV}_{p_i} \tag{33}$$

Figure 4 shows an example of a set of base points and direction vectors which are used to describe the location of the unknown boundary $\partial\Omega_T$. Note that the selection of their location and orientation clearly depends on the geometry of each problem.

Hence, given a set of surface points, the location of the unknown boundary $\partial\Omega_T$ is interpolated with a smooth function. We consider radial basis functions (RBFs) because they impose few restrictions on the geometry of the interpolation points which do not need to lie on a regular grid, and because they provide a smooth interpolation [14–19]. Therefore, the direct heat transfer problem domain is perfectly defined.

Finally, since the direct problem must be solved several times for each inverse problem iteration, we use remeshing techniques in order to discretize each different geometry.

Copyright © 2005 John Wiley & Sons, Ltd.

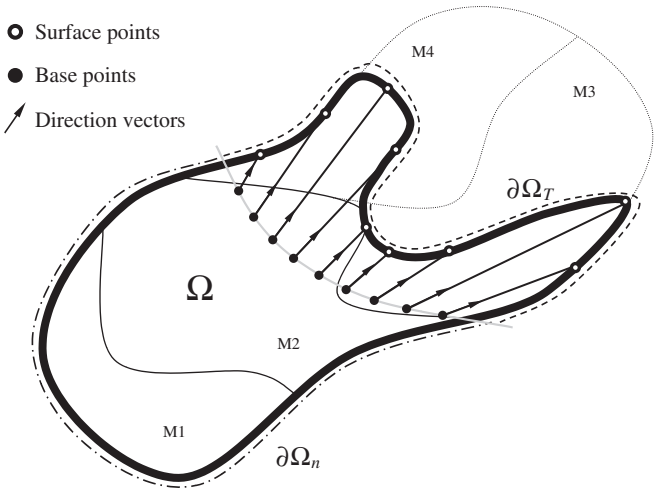

Figure 4. Schematic of the geometry parameterization.

4.1. Radial basis functions

The problem consists in finding an interpolation function $\Phi(\mathbf{x})$ given a set of n_{sp} points on the unknown boundary $\partial\Omega_T$ (where $\Phi = 0$) and a set of n_{ip} points inside the volume Ω (where $\Phi < 0$). For this purpose, we choose RBFs defined by

$$\Phi(\mathbf{x}) = q(\mathbf{x}) + \sum_{i=1}^{n} \alpha_i R_{(\|\mathbf{x}-\mathbf{x}^i\|)} \tag{34}$$

where $n = n_{sp} + n_{ip}$; $q_{(\mathbf{x})}$ is a low degree polynomial; α_i are real numbers; and R is the basis function [14–16, 21] of which some examples are given below

1. Biharmonic spline (for fitting functions of three variables), $R_{(r)} = r = \|\mathbf{x} - \mathbf{x}^i\|$.
2. Thin plate spline (for fitting smooth functions of two variables), $R_{(r)} = r^2 \log(r)$.
3. Gaussian (for neural networks), $R_{(r)} = \mathrm{e}^{-cr^2}$.
4. Triharmonic spline (for fitting functions of three variables), $R_{(r)} = r^3$.
5. Multiquadratic (for fitting topographical data), $R_{(r)} = \sqrt{r^2 + c^2}$.

Among them, as we justify in Section 5, we use *thin plate spline* functions on $\mathbb{R}^2$ defined by

$$R_{(r)} = r^2 \log(r) \tag{35}$$

$$q_{(\mathbf{x})} = q_{(x_1,x_2)} = d_0 + d_1 x_1 + d_2 x_2 \tag{36}$$

As $\Phi(\mathbf{x})$ is chosen from the Beppo–Levi space of distributions on $\mathbb{R}^2$ with square integrable second derivative, some conditions must be imposed on α_i

$$\sum_{i=1}^{n} \alpha_i = \sum_{i=1}^{n} \alpha_i x_1^i = \sum_{i=1}^{n} \alpha_i x_2^i = 0 \tag{37}$$

Copyright © 2005 John Wiley & Sons, Ltd.

Therefore, the coefficients α_i and d_j are obtained from the following system of equations:

$$\begin{bmatrix} \mathbf{A} & \mathbf{Q} \\ \mathbf{Q}^{\mathrm{T}} & \mathbf{0} \end{bmatrix} \begin{pmatrix} \boldsymbol{\alpha} \\ \mathbf{d} \end{pmatrix} = \begin{pmatrix} \boldsymbol{\Phi} \\ \mathbf{0} \end{pmatrix} \tag{38}$$

where

$$\mathrm{A}_{ij} = \|\mathbf{x}^i - \mathbf{x}^j\|^2 \log(\|\mathbf{x}^i - \mathbf{x}^j\|), \quad \mathbf{A} \in \mathbb{R}^{n \times n} \tag{39}$$

$$\mathbf{Q} = \begin{bmatrix} 1 & x_1^1 & x_2^1 \\ \vdots & \vdots & \vdots \\ 1 & x_1^n & x_2^n \end{bmatrix} \in \mathbb{R}^{n \times 3} \tag{40}$$

$$\boldsymbol{\alpha}^{\mathrm{T}} = (\alpha_1 \quad \cdots \quad \alpha_n) \in \mathbb{R}^n \tag{41}$$

$$\mathbf{d}^{\mathrm{T}} = (d_0 \quad d_1 \quad d_2) \in \mathbb{R}^3 \tag{42}$$

$$\boldsymbol{\Phi}^{\mathrm{T}} = (\Phi_{(\mathbf{x}^1)} \quad \cdots \quad \Phi_{(\mathbf{x}^n)}) \in \mathbb{R}^n \tag{43}$$

Note that $\Phi_{(\mathbf{x}^i)}$ is equal to zero except for the n_{ip} interior points.

4.2. Remeshing algorithm

As bidimensional problems are our focus, we implemented the following simple but effective remeshing algorithm:

1. The starting point is a structured mesh of quadrilateral elements, where different materials may be defined. According to the definition of the interpolation function $\Phi(\mathbf{x})$, there will be some nodes located inside the volume Ω, where $\Phi<0$, and some located outside, where $\Phi>0$. Remember that the unknown boundary $\partial\Omega_T$ is defined as $\Phi = 0$.
2. All the elements with three or four nodes inside the volume Ω ($\Phi<0$) remain in the mesh (Step 1 of Figure 5).
3. A set of 'boundary nodes' is defined. These nodes are the white ($\Phi<0$) and grey ($\Phi>0$) nodes of Figure 5.
4. The nodes that belong to the set of 'boundary nodes' and that are located outside the volume Ω ($\Phi>0$) are collapsed generating triangular elements (Step 2 of Figure 5).
5. Each node that belongs to the set of 'boundary nodes' is moved to the nearest point of the unknown boundary $\partial\Omega_T$ (Step 3 of Figure 5). The nearest point is calculated solving the following non-linear optimization problem:

$$\min_{\mathbf{x}} \quad f(\mathbf{x}) = \tfrac{1}{2}\|\mathbf{x} - \mathbf{x}^{\mathrm{Node}}\|^2 \tag{44}$$

$$\text{subject to} \quad \Phi(\mathbf{x}) = 0 \tag{45}$$

where $\mathbf{x}^{\mathrm{Node}}$ are the co-ordinates of the node that is being moved.

Copyright © 2005 John Wiley & Sons, Ltd.

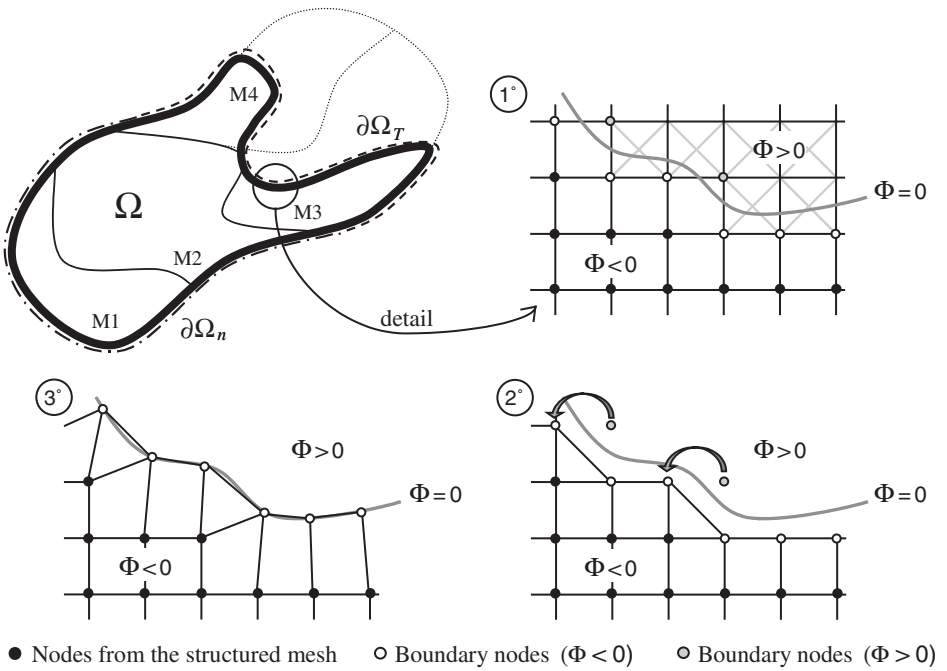

Figure 5. Schema of the remeshing algorithm.

5. INDUSTRIAL APPLICATION

In this section, we develop the industrial application of estimating the location of the 1150°C isotherm in a blast furnace hearth, based on measurements of thermocouples located inside it.

Regarding the direct problem, we model a vertical section of the lining (Figure 6) with axisymmetric finite elements because the geometry of the blast furnace hearth is rotationally symmetric about an axis and is subjected to axisymmetric cooling conditions (Table I). The finite element mesh has around 5000 isoparametric elements depending on the geometry solved for each inverse problem iteration. Table II shows the temperature dependence of the hearth refractories thermal properties considered in the direct model.

Regarding the inverse geometry problem, there are 28 thermocouples located inside the blast furnace hearth section (as shown in Figure 6) so the number of observations (n_{obs}) is equal to 28. The number of parameters used to parameterize the location of the unknown boundary (n_p) is chosen to be 7. As stated in the previous section, the selection of a set of base points and direction vectors depends on the geometry of each problem. In our problem, we select them depending also on the position of the thermocouples.

Figure 7 shows the set of base points and direction vectors which are used to describe the location of the 1150°C isotherm, where the set of surface points is interpolated using *thin plate spline* RBFs. Thin plate spline functions were chosen over the examples given in Section 4.1, visually comparing the location and smoothness of the interpolated boundary for a given set of surface points. Figure 8 shows the comparison between the biharmonic spline function and

Copyright © 2005 John Wiley & Sons, Ltd.

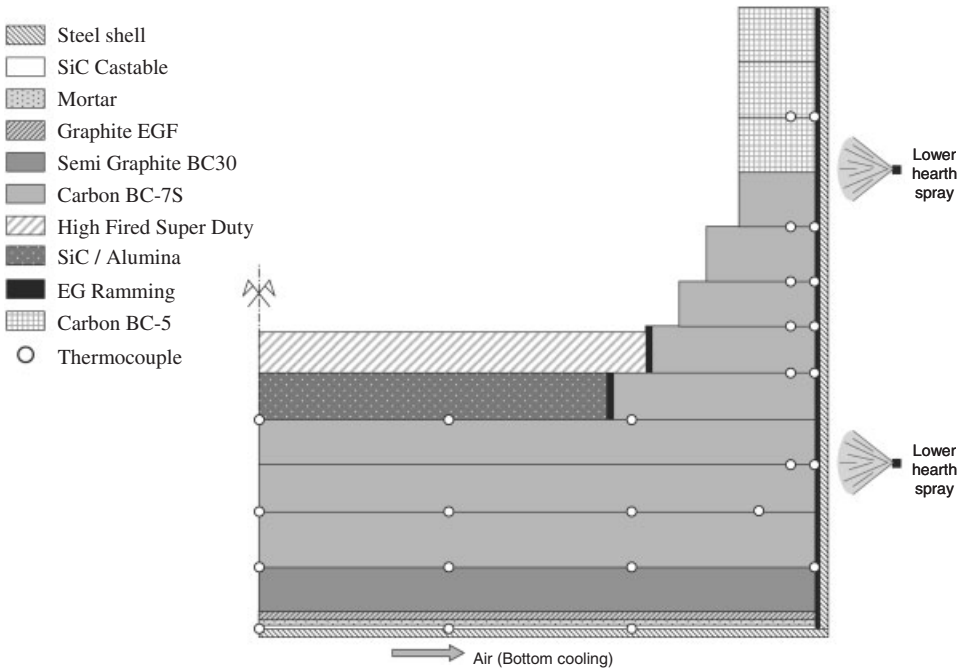

Figure 6. Vertical section of the blast furnace hearth.

Table I. Cooling conditions.

Cooling zone	Convective cooling parameters	
Lower hearth spray	$h_{\text{water}} = 150 \dfrac{W}{m^{2\circ}\text{C}}$	$T_{\text{water}} = 20^{\circ}\text{C}$
Bottom cooling	$h_{\text{air}} = \left(152.5 - 169.9\dfrac{r}{r_{\max}} + 45.3\left[\dfrac{r}{r_{\max}}\right]^2\right)\dfrac{W}{m^{2\circ}\text{C}}$	$T_{\text{air}} = \left(26 + 22\dfrac{r}{r_{\max}}\right)^{\circ}\text{C}$

the thin plate spline function, and it can be seen that the thin plate spline is better for the purposes of our industrial application.

In order to validate the solution of the algorithm against measurement uncertainties, we simulate measurements with different levels of noise following these steps:

1. To define a 'real geometry' described by a set of geometry parameters $\mathbf{p}^{\text{Real}}$.
2. To calculate the temperature observations that correspond to the 'real geometry', $\mathbf{T}^{\text{Real}}$, assuming error free measurements.
3. To simulate measurements with different levels of noise (noise $= 5, 10, 15\%$) as follows:

$$T_i^{\text{Obs}} = T_i^{\text{Real}}(1 + \xi \cdot \text{noise}) \tag{46}$$

where $\xi \in [-1; +1]$ is a uniformly distributed random disturbance.

Copyright © 2005 John Wiley & Sons, Ltd.

Table II. Material properties.

Refractories	Thermal conductivity	
SiC Castable	20.00 W/mK	
Mortar	1.00 W/mK	
Graphite EGF	$T = 303$ K	150.0 W/mK
	$T = 773$ K	90.0 W/mK
	$T = 1273$ K	60.0 W/mK
Semi graphite BC-30	$T = 293$ K	36.00 W/mK
	$T = 473$ K	34.80 W/mK
	$T = 673$ K	33.10 W/mK
	$T = 873$ K	32.00 W/mK
	$T = 1073$ K	31.50 W/mK
Carbon BC-7S	$T = 873$ K	14.12 W/mK
	$T = 1073$ K	14.99 W/mK
	$T = 1273$ K	15.63 W/mK
	$T = 1473$ K	16.09 W/mK
SiC/alumina	7.20 W/mK	
High fired super duty	$T = 673$ K	1.300 W/mK
	$T = 873$ K	1.400 W/mK
	$T = 1073$ K	1.500 W/mK
	$T = 1473$ K	1.600 W/mK
EG ramming	$T = 293$ K	25.00 W/mK
	$T = 473$ K	20.00 W/mK
	$T = 873$ K	11.00 W/mK
	$T = 1273$ K	8.00 W/mK
	$T = 1573$ K	7.00 W/mK
Carbon BC-5	$T = 873$ K	16.96 W/mK
	$T = 1073$ K	17.66 W/mK
	$T = 1273$ K	18.13 W/mK
	$T = 1473$ K	18.36 W/mK

As measurement uncertainties not only come from measurement errors but also from differences between the model and reality (like thermal contact resistants between refractories blocks, parameters of the boundary conditions, material properties, real location of the measurements, and others), we use a uniformly distributed random disturbance trying to be general.

Then, we solve the inverse geometry heat transfer problem for each set of observations, using as initial guess the regularization geometry $\mathbf{p}^0 = \mathbf{p}^{\Delta}$, and we evaluate the following relative errors:

$$\varepsilon_{\text{obs}} = \frac{\|\mathbf{T}_{(\mathbf{p}^{\text{Iter}})} - \mathbf{T}^{\text{Obs}}\|}{\|\mathbf{T}^{\text{Obs}}\|} \tag{47}$$

$$\varepsilon_{\text{geom}} = \frac{\|\mathbf{p}^{\text{Iter}} - \mathbf{p}^{\text{Real}}\|}{\|\mathbf{p}^{\text{Real}}\|} \tag{48}$$

Copyright © 2005 John Wiley & Sons, Ltd.

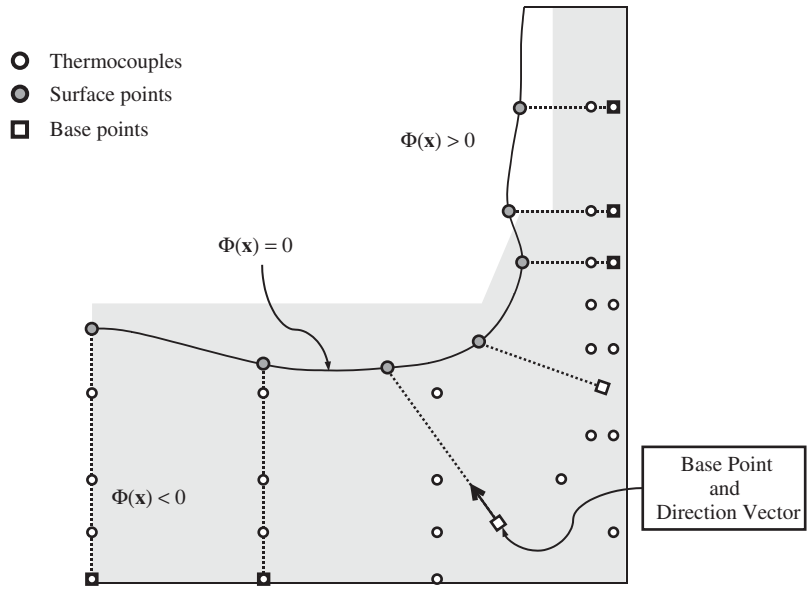

Figure 7. Parameterization of the unknown boundary location.

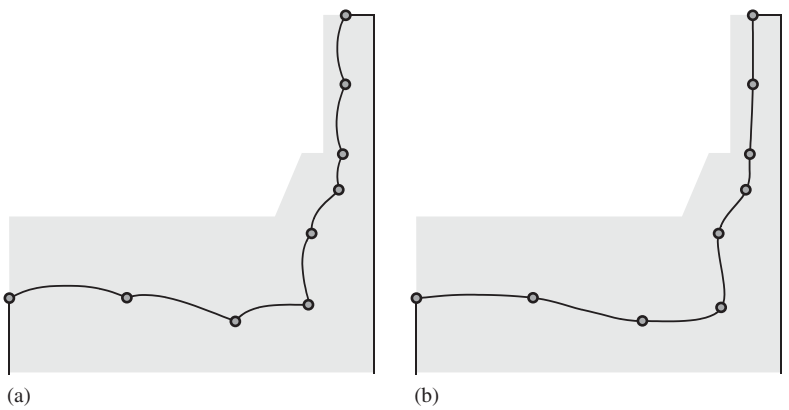

Figure 8. Parameterization of the unknown boundary location with different radial basis functions: (a) biharmonic spline; and (b) thin plate spline.

Finally, we focus on three aspects of the problem:

- The determination of the optimal regularization matrix for a problem with no geometry restrictions.
- The algorithm behaviour when the problem is subjected to some geometry restrictions.
- The error behaviour of the solution.

Copyright © 2005 John Wiley & Sons, Ltd.

Table III. Problem with no geometry restrictions—noise = 0%.

Regularization			ε_{geom} (%)		Iterations	
w_0	w_1	w_2	Mean	Std. Dev.	Mean	Std. Dev.
1.00	0.00	0.00	0.455	—	4	—
0.00	1.00	0.00	0.397	—	4	—
0.00	0.00	1.00	0.352	—	4	—
0.00	0.50	0.50	0.373	—	4	—
0.50	0.50	0.00	0.537	—	4	—
0.50	0.00	0.50	0.513	—	4	—

Table IV. Problem with no geometry restrictions—noise = 5%.

Regularization			ε_{geom} (%)		Iterations	
w_0	w_1	w_2	Mean	Std. Dev.	Mean	Std. Dev.
1.00	0.00	0.00	5.021	2.125	3.10	0.32
0.00	1.00	0.00	4.374	2.077	3.30	0.48
0.00	0.00	1.00	3.894	1.885	3.30	0.48
0.00	0.50	0.50	4.139	2.182	3.40	0.70
0.50	0.50	0.00	4.472	2.400	3.20	0.42
0.50	0.00	0.50	4.399	1.902	3.20	0.42

5.1. Determination of the optimal regularization matrix

We analyse the behaviour of the algorithm on different regularization matrices. For this purpose, we propose six regularization matrices as linear combinations of $\mathbf{L}_0$, $\mathbf{L}_1$, $\mathbf{L}_2$ (Equation (19)) and solve the inverse geometry heat transfer problem for each case, assuming a problem with no geometry restrictions. Since the noise is generated using random disturbances, ten simulations were performed for each noise level (details in Appendix A).

Tables IV, V and VI show the mean and standard deviation of the relative error ε_{obs} and the number of iterations required to solve the problem for each set of weighting factors (w_0, w_1, w_2) and for each noise level. Table III shows results for error free measurements.

Analysing these results, we conclude that:

- As is expected, the error on the estimated geometry, ε_{geom}, increases as the noise increases.
- The algorithm is equally stable for different regularization matrices when measurements have a low level of noise because ε_{geom} remains stable in all cases (Table IV).
- The optimal regularization matrix appears to be $(0.00, 0.00, 1.00)$ because the solutions have the lowest mean and standard deviation of the error on the estimated geometry, ε_{geom}, particularly when measurements have a high level of noise (Tables V and VI).
- Even though 15% is a high level of noise, the geometry is estimated with good accuracy in the context of the industrial application (Figure 9).

5.2. The bound-constrained problem

We also analyse the behaviour of the algorithm on different regularization matrices but, as our aim is to consider the bound-constrained problem, we work on a set of observations for

Copyright © 2005 John Wiley & Sons, Ltd.

Table V. Problem with no geometry restrictions—noise = 10%.

Regularization			ε_{geom} (%)		Iterations	
w_0	w_1	w_2	Mean	Std. Dev.	Mean	Std. Dev.
1.00	0.00	0.00	8.236	2.184	3.30	0.67
0.00	1.00	0.00	7.678	2.708	3.20	0.42
0.00	0.00	1.00	6.803	1.464	2.80	0.42
0.00	0.50	0.50	8.787	3.895	3.10	0.57
0.50	0.50	0.00	7.837	3.214	3.30	0.67
0.50	0.00	0.50	7.599	2.570	3.00	0.47

Table VI. Problem with no geometry restrictions—noise = 15%.

Regularization			ε_{geom} (%)		Iterations	
w_0	w_1	w_2	Mean	Std. Dev.	Mean	Std. Dev.
1.00	0.00	0.00	11.475	4.191	3.00	0.00
0.00	1.00	0.00	10.485	3.157	2.70	0.48
0.00	0.00	1.00	10.106	1.445	2.30	0.48
0.00	0.50	0.50	10.376	3.159	2.60	0.52
0.50	0.50	0.00	10.987	3.513	2.90	0.32
0.50	0.00	0.50	11.128	3.458	2.60	0.52

which the iterative solution process yields unfeasible solutions due to its instability. This is the case of solving 'Simulation 4 - noise = 10%' with no geometry restrictions (see Appendix A), against which the solution of the bound-constrained problem is compared in Table VII.

Finally, we repeat the ten simulations performed for noise = 10% but considering some geometry restrictions, and Table VIII shows the mean and standard deviation of the relative error ε_{obs} and the number of iterations required for each set of weighting factors (w_0, w_1, w_2).

Analysing these results, we conclude that:

- The solution is clearly improved and stabilized for all the regularization matrices when the bound-constrained algorithm is used (Table VII).
- The optimal regularization matrix appears to be (0.00, 0.00, 1.00), as in the problem with no geometry restrictions (Tables V and VIII).
- More iterations are needed to reach convergence, which is an expected conclusion because the constraints are iteratively imposed.
- The geometry is estimated with good accuracy in the context of the industrial application (Figure 10).

5.3. Error behaviour of the solution

We analyse the error behaviour of the solution considering the optimal regularization matrix (0.00, 0.00, 1.00) and 'Simulation 4—noise = 10%' (see Appendix A), simulation for which the iterative solution process yields unfeasible solutions. Moreover, as this behaviour depends on multiple factors, we divide the study in three parts.

Copyright © 2005 John Wiley & Sons, Ltd.

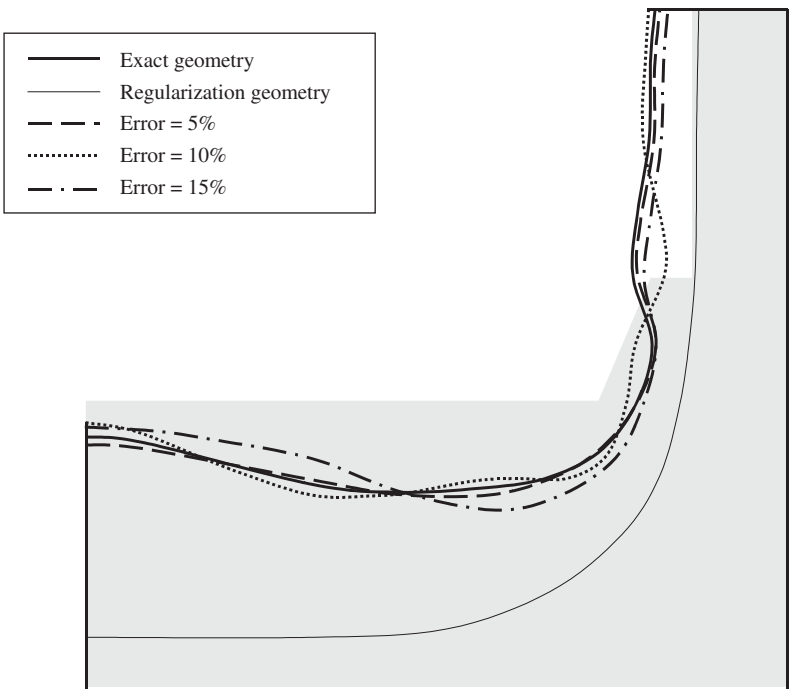

Figure 9. Estimated geometry for different levels of noise, using the optimal regularization matrix.

Table VII. Results of Simulation 4—noise = 10%.

Regularization			With no geometry restrictions		With geometry restrictions	
w_0	w_1	w_2	ε_{geom} (%)	Iter	ε_{geom} (%)	Iter
1.00	0.00	0.00	11.938	3	9.855	4
0.00	1.00	0.00	11.686	3	7.198	4
0.00	0.00	1.00	7.760	3	6.366	5
0.00	0.50	0.50	17.152	3	4.919	6
0.50	0.50	0.00	12.266	3	8.063	4
0.50	0.00	0.50	12.840	3	5.759	5

In the first part of the study, we analyse the error behaviour of the solution calculating an appropriate step length (Section 3.1) and considering no geometry restrictions. In the second part of the study, we also calculate an appropriate step length but this time with some geometry restrictions. Finally, in the third part of the study, we use a constant step length equal to 1.00 in order to evaluate the importance of calculating an appropriate step length.

Figures 11–13 show the evolution of the relative errors (ε_{obs} and ε_{geom}) during the iterative process.

Copyright © 2005 John Wiley & Sons, Ltd.

Table VIII. Problem with geometry restrictions—noise = 10%.

Regularization			ε_{geom} (%)		Iterations	
w_0	w_1	w_2	Mean	Std. Dev.	Mean	Std. Dev.
1.00	0.00	0.00	8.108	1.814	3.80	1.32
0.00	1.00	0.00	7.370	3.000	3.90	1.20
0.00	0.00	1.00	6.578	1.379	3.50	1.51
0.00	0.50	0.50	7.285	2.946	3.70	1.34
0.50	0.50	0.00	7.356	2.853	3.50	0.71
0.50	0.00	0.50	7.006	1.634	3.70	1.25

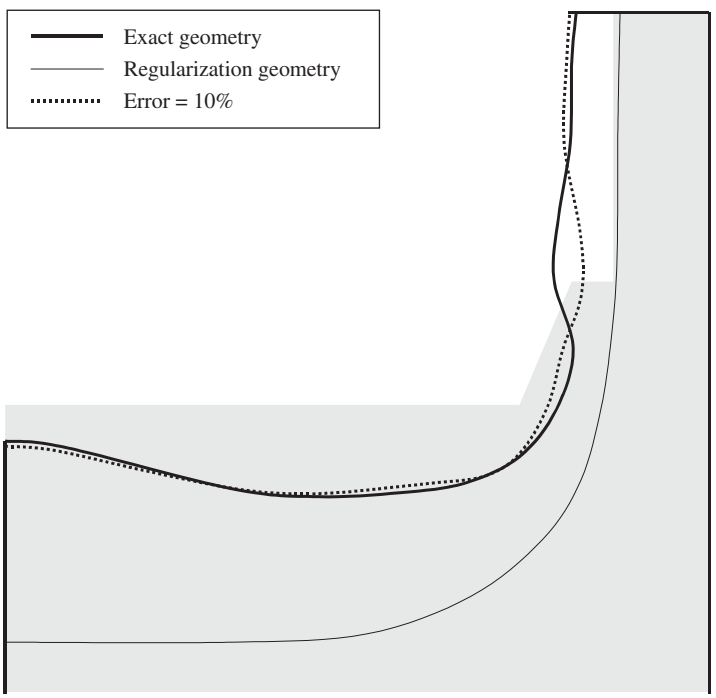

Figure 10. Geometry estimated by the bound-constrained algorithm, using the optimal regularization matrix.

Analysing these results, we conclude that:

- The typical instability of ill-posed problems, which causes ε_{geom} to increase after some iterations while ε_{obs} always decreases, clearly occurs in the first case (Figure 11). This confirms the use of the discrepancy principle as a stopping rule for the iterative process, as we explained in Section 3.1.4.
- The solution is strongly stabilized when the bound-constrained algorithm is used (Figure 12). Even in this case, the discrepancy principle is an efficient stopping rule for the iterative process.

Copyright © 2005 John Wiley & Sons, Ltd.

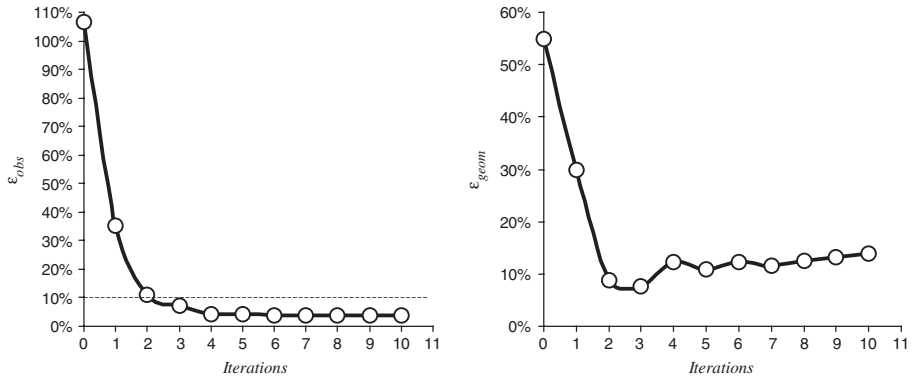

Figure 11. Error behaviour of the solution, calculating an appropriate step length and considering no geometry restrictions.

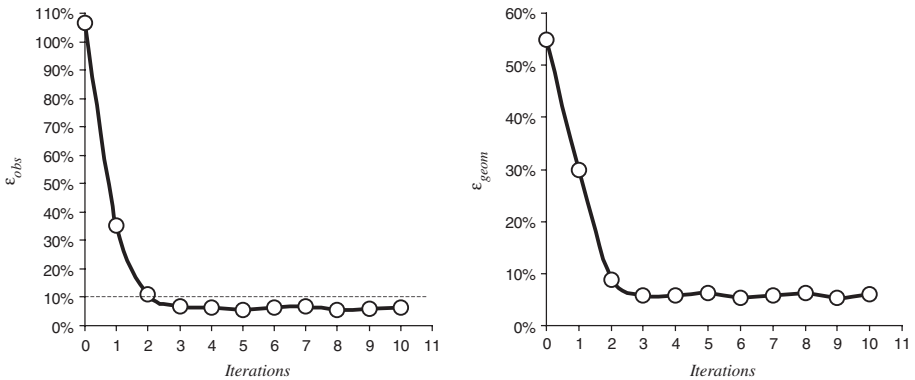

Figure 12. Error behaviour of the solution, calculating an appropriate step length and considering some geometry restrictions.

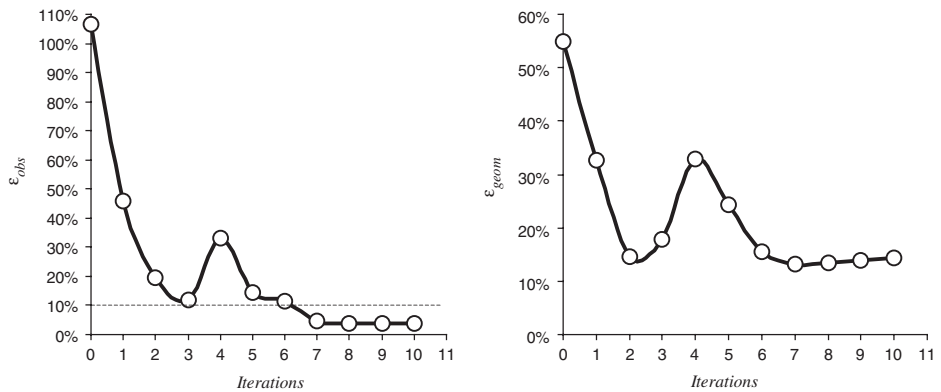

Figure 13. Error behaviour of the solution, using a step length equal to 1.00 and considering no geometry restrictions.

Copyright © 2005 John Wiley & Sons, Ltd.

- The behaviour of the solution is not good when a constant step length equal to 1.00 is used (Figure 13). Therefore, as is expected, the selection of an appropriate step length makes sense due to the highly non-linear nature of the problem.

6. CONCLUSIONS

We have developed an inverse geometry heat transfer model for estimating the location of the 1150°C isotherm in a blast furnace hearth. The observations of the inverse problem are temperature measurements at points inside the object and the unknown is the geometry of the volume where the problem is defined. We have considered not only the problem with no geometry restrictions but also the bound-constrained problem. Due to the typical instability of ill-posed problems and the non-linearity of our inverse problem, we have used the iteratively regularized Gauss–Newton method.

The inverse geometry problem is based on a radial basis functions geometry representation. For this purpose, the location of the unknown boundary has been parameterized by a set of parameters and described with radial basis functions. We have considered RBFs because they impose few restrictions on the geometry and because they provide a smooth interpolation.

The behaviour of the algorithm on different regularization matrices has been studied analysing its stability against simulated measurements with different levels of noise. Moreover, since the noise has been generated using random disturbances, ten simulations were performed for each noise level.

We can conclude, from the results of the analysed cases, that the optimal regularization matrix appears to be $\mathbf{L}_2$ (the discrete approximation of the second derivative operator) for both the problem with no geometry restrictions and the bound-constrained problem. We also conclude that the solution is clearly improved and stabilized if the bound-constrained algorithm is used when the iterative solution process yields unfeasible solutions due to the instability of the problem.

From our numerical experimentation, we have confirmed that a stopping rule for the iterative process must be used, and that the selection of an appropriate step length makes sense due to the highly non-linear nature of the problem.

Finally, as the geometry is estimated with good accuracy in the context of the industrial application, we conclude that the algorithm developed is a reliable tool for estimating the location of the 1150°C isotherm in a blast furnace hearth.

APPENDIX A: NUMERICAL SIMULATIONS

Ten simulations were performed for each noise level, and results are shown in the following tables:

- Table AI: Results for each set of weighting factors (w_0, w_1, w_2) using a level of noise equal to 5% and considering no geometry restrictions.
- Table AII: Results for each set of weighting factors (w_0, w_1, w_2) using a level of noise equal to 10% and considering no geometry restrictions.
- Table AIII: Results for each set of weighting factors (w_0, w_1, w_2) using a level of noise equal to 15% and considering no geometry restrictions.

Copyright © 2005 John Wiley & Sons, Ltd.

Table AI. Problem with no geometry restrictions—noise = 5%.

	Simulation	1	2	3	4	5	6	7	8	9	10
$w_0 = 1.00$	ε_{obs} (%)	2.698	3.628	2.008	3.032	3.051	3.822	1.826	3.618	2.023	3.257
$w_1 = 0.00$	ε_{geom} (%)	4.317	8.668	7.724	4.329	2.064	4.340	3.464	5.324	6.906	3.076
$w_2 = 0.00$	Iter	3	3	3	3	3	3	3	3	4	3
$w_0 = 0.00$	ε_{obs} (%)	3.041	3.273	1.890	2.884	2.094	3.372	1.789	3.296	2.108	2.650
$w_1 = 1.00$	ε_{geom} (%)	4.816	8.413	6.513	4.142	1.154	2.467	3.182	4.486	5.337	3.234
$w_2 = 0.00$	Iter	3	3	3	3	4	3	3	4	4	3
$w_0 = 0.00$	ε_{obs} (%)	2.925	3.027	1.913	3.169	2.093	2.459	2.814	2.108	1.239	2.479
$w_1 = 0.00$	ε_{geom} (%)	2.807	7.130	4.064	5.316	1.614	2.814	4.076	2.872	6.443	1.808
$w_2 = 1.00$	Iter	3	3	3	3	4	4	3	3	4	3
$w_0 = 0.00$	ε_{obs} (%)	3.666	3.127	1.941	2.794	2.005	3.650	2.294	2.017	1.548	2.471
$w_1 = 0.50$	ε_{geom} (%)	4.631	7.669	4.936	4.133	1.084	4.214	2.341	3.390	7.336	1.655
$w_2 = 0.50$	Iter	3	3	3	3	4	3	5	3	4	3
$w_0 = 0.50$	ε_{obs} (%)	2.729	3.406	1.884	2.943	2.120	3.320	1.796	3.531	2.260	2.710
$w_1 = 0.50$	ε_{geom} (%)	4.395	8.784	7.021	4.227	1.558	0.800	3.319	5.119	5.956	3.512
$w_2 = 0.00$	Iter	3	3	3	3	4	3	3	3	4	3
$w_0 = 0.50$	ε_{obs} (%)	3.647	3.251	1.689	2.886	2.039	3.639	2.860	3.006	1.881	2.378
$w_1 = 0.00$	ε_{geom} (%)	4.571	8.005	5.083	4.200	1.159	4.627	4.269	4.391	5.820	1.863
$w_2 = 0.50$	Iter	3	3	3	3	4	3	3	3	4	3

Table AII. Problem with no geometry restrictions—noise = 10%.

	Simulation	1	2	3	4	5	6	7	8	9	10
$w_0 = 1.00$	ε_{obs} (%)	5.966	4.386	6.466	6.267	6.292	4.009	6.998	3.375	5.795	6.707
$w_1 = 0.00$	ε_{geom} (%)	5.807	6.545	8.004	11.93	9.737	6.682	7.466	5.879	11.21	9.094
$w_2 = 0.00$	Iter	3	3	3	3	5	3	4	3	3	3
$w_0 = 0.00$	ε_{obs} (%)	5.949	4.154	4.800	6.228	6.348	3.956	6.272	3.425	5.250	5.749
$w_1 = 1.00$	ε_{geom} (%)	5.962	7.960	4.115	11.68	11.13	9.265	6.188	5.055	10.01	5.403
$w_2 = 0.00$	Iter	3	3	3	3	4	3	4	3	3	3
$w_0 = 0.00$	ε_{obs} (%)	6.110	6.100	6.196	7.009	5.691	5.768	4.801	6.147	4.909	7.018
$w_1 = 0.00$	ε_{geom} (%)	7.527	5.387	5.850	7.760	8.388	4.499	5.107	7.170	8.589	7.752
$w_2 = 1.00$	Iter	3	3	3	3	3	3	3	2	3	2
$w_0 = 0.00$	ε_{obs} (%)	7.147	5.072	7.667	5.074	7.216	3.250	6.980	3.749	5.100	7.531
$w_1 = 0.50$	ε_{geom} (%)	10.29	6.739	6.500	17.15	12.78	4.064	8.023	4.887	9.340	8.082
$w_2 = 0.50$	Iter	3	3	3	3	4	3	4	3	3	2
$w_0 = 0.50$	ε_{obs} (%)	5.942	4.312	5.489	7.483	6.427	5.610	6.079	3.469	5.560	5.907
$w_1 = 0.50$	ε_{geom} (%)	5.652	6.387	6.004	12.26	14.06	5.803	5.803	5.087	10.54	6.753
$w_2 = 0.00$	Iter	3	3	3	3	5	3	4	3	3	3
$w_0 = 0.50$	ε_{obs} (%)	6.215	6.624	7.785	6.485	5.463	3.138	6.541	3.303	5.417	8.080
$w_1 = 0.00$	ε_{geom} (%)	4.403	7.451	7.426	12.84	8.100	4.765	6.873	5.281	10.08	8.758
$w_2 = 0.50$	Iter	3	3	3	3	3	3	4	3	3	2

Copyright © 2005 John Wiley & Sons, Ltd.

Table AIII. Problem with no geometry restrictions—noise = 15%.

	Simulation	1	2	3	4	5	6	7	8	9	10
$w_0 = 1.00$	ε_{obs} (%)	4.956	8.232	8.354	5.749	11.65	7.625	5.216	7.323	6.427	5.833
$w_1 = 0.00$	ε_{geom} (%)	10.77	8.089	19.96	10.04	13.06	5.808	13.63	7.887	9.855	15.62
$w_2 = 0.00$	Iter	3	3	3	3	3	3	3	3	3	3
$w_0 = 0.00$	ε_{obs} (%)	9.705	8.820	8.378	10.59	8.893	4.77	4.736	7.069	6.115	6.792
$w_1 = 1.00$	ε_{geom} (%)	12.22	8.227	16.51	12.05	9.858	5.213	9.639	9.069	8.648	13.40
$w_2 = 0.00$	Iter	2	3	3	2	3	3	3	2	3	3
$w_0 = 0.00$	ε_{obs} (%)	6.144	11.73	11.68	6.908	12.23	10.00	5.055	8.342	10.39	6.205
$w_1 = 0.00$	ε_{geom} (%)	9.577	9.076	12.70	10.51	11.36	8.353	8.311	10.10	11.59	9.456
$w_2 = 1.00$	Iter	2	3	2	2	2	2	3	2	2	3
$w_0 = 0.00$	ε_{obs} (%)	6.274	10.24	8.183	8.017	8.124	10.19	5.347	7.141	5.125	5.884
$w_1 = 0.50$	ε_{geom} (%)	9.813	7.037	18.30	10.90	5.564	8.614	8.854	8.535	11.94	11.19
$w_2 = 0.50$	Iter	2	3	3	2	3	2	3	2	3	3
$w_0 = 0.50$	ε_{obs} (%)	4.576	8.248	8.168	5.149	9.834	5.497	4.632	10.52	6.275	5.919
$w_1 = 0.50$	ε_{geom} (%)	9.850	5.257	18.66	10.56	11.58	6.027	11.42	9.338	9.531	14.63
$w_2 = 0.00$	Iter	3	3	3	3	3	3	3	2	3	3
$w_0 = 0.50$	ε_{obs} (%)	8.865	8.796	8.352	9.639	9.067	11.49	5.160	7.735	6.141	6.775
$w_1 = 0.00$	ε_{geom} (%)	11.66	6.626	19.81	11.88	10.38	9.677	10.41	9.063	9.563	12.18
$w_2 = 0.50$	Iter	2	3	3	2	3	2	3	2	3	3

Table AIV. Problem with geometry restrictions—noise = 10%.

	Simulation	1	2	3	4	5	6	7	8	9	10
$w_0 = 1.00$	ε_{obs} (%)	5.966	7.392	6.466	7.496	6.292	4.009	6.998	3.375	5.795	6.707
$w_1 = 0.00$	ε_{geom} (%)	5.807	7.344	8.004	9.855	9.737	6.682	7.466	5.879	11.21	9.094
$w_2 = 0.00$	Iter	3	7	3	4	5	3	4	3	3	3
$w_0 = 0.00$	ε_{obs} (%)	5.912	6.181	4.800	7.353	6.348	3.956	6.272	3.425	5.250	5.749
$w_1 = 1.00$	ε_{geom} (%)	11.83	3.493	4.115	7.198	11.13	9.265	6.188	5.055	10.01	5.403
$w_2 = 0.00$	Iter	6	6	3	4	4	3	4	3	3	3
$w_0 = 0.00$	ε_{obs} (%)	6.572	4.906	6.196	5.474	5.691	5.768	4.801	6.147	4.909	7.018
$w_1 = 0.00$	ε_{geom} (%)	6.474	5.580	5.850	6.366	8.388	4.499	5.107	7.170	8.589	7.752
$w_2 = 1.00$	Iter	4	7	3	5	3	3	3	2	3	2
$w_0 = 0.00$	ε_{obs} (%)	7.147	6.035	7.667	6.075	7.216	3.250	6.980	3.749	5.100	7.531
$w_1 = 0.50$	ε_{geom} (%)	10.29	3.957	6.500	4.919	12.78	4.064	8.023	4.887	9.340	8.082
$w_2 = 0.50$	Iter	3	6	3	6	4	3	4	3	3	2
$w_0 = 0.50$	ε_{obs} (%)	5.942	7.496	5.489	7.914	6.427	5.610	6.079	3.469	5.560	5.907
$w_1 = 0.50$	ε_{geom} (%)	5.652	5.778	6.004	8.063	14.06	5.803	5.803	5.087	10.54	6.753
$w_2 = 0.00$	Iter	3	4	3	4	5	3	4	3	3	3
$w_0 = 0.50$	ε_{obs} (%)	7.862	6.561	7.785	7.236	5.463	3.138	6.541	3.303	5.417	8.080
$w_1 = 0.00$	ε_{geom} (%)	6.592	6.415	7.426	5.759	8.100	4.765	6.873	5.281	10.08	8.758
$w_2 = 0.50$	Iter	5	6	3	5	3	3	4	3	3	2

Copyright © 2005 John Wiley & Sons, Ltd.

- Table AIV: Results for each set of weighting factors (w_0, w_1, w_2) using a level of noise equal to 10% and considering geometry restrictions.

ACKNOWLEDGEMENTS

We thankfully acknowledge the financial support and the information provided by SIDERAR (San Nicolás, Argentina).

REFERENCES

1. Wawrzynek A, Kogut M, Nowak A, Delpak R, Hu C-W. Regularization method in geometrical inverse heat conduction problems—preliminary report. *CD-ROM with Proceedings of ECCOMAS 2000*, Barcelona, 2000.
2. Park HM, Shin HJ. Shape identification for natural convection problems using the adjoint variable method. *Journal of Computational Physics* 2003; **186**:198–211.
3. Kwag D-S, Park I-S, Kim W-S. Inverse geometry problem of estimating the phase front motion of ice in a thermal storage system. *Inverse Problems in Science and Engineering* 2004; **12**(1):1–15.
4. Huang C-H. An inverse geometry problem in estimating frost growth on an evaporating tube. *Heat and Mass Transfer* 2002; **38**:615–623.
5. Ganapathysubramanian S, Zabaras N. A continuum sensitivity method for finite thermo-inelastic deformations with applications to the design of hot forming processes. *International Journal for Numerical Methods in Engineering* 2002; **55**:1391–1437.
6. Engl HW, Hanke M, Neubauer A. *Regularization of Inverse Problems*. Kluwer Academic Publishers: Dordrecht, 1996.
7. Alifanov OM. *Inverse Heat Transfer Problems*. Springer: Berlin, 1994.
8. Bakushinskii AB. The problem of the convergence of the iteratively regularized Gauss–Newton method. *Computational Mathematics and Mathematical Physics* 1992; **32**(9):1353–1359.
9. Kaltenbacher B. On convergence rates of some iterative regularization methods for an inverse problem for nonlinear parabolic equation connected with continuous casting of steel. *Journal of Inverse and Ill-Posed Problems* 1999; **7**(2):145–164.
10. Jin QN. The analysis of a discrete scheme of the iteratively regularized Gauss–Newton method. *Inverse Problems* 2000; **16**:1457–1476.
11. Jin QN. On the iteratively regularized Gauss–Newton method for solving nonlinear ill-posed problems. *Mathematics of Computation* 2000; **69**(232):1603–1623.
12. Kaltenbacher B, Neubauer A, Ramm AG. Convergence rates of the continuous regularized Gauss–Newton method. *Journal of Inverse and Ill-Posed Problems* 2002; **10**(3):261–280.
13. Doicu A, Schreier F, Hess M. Iteratively regularized Gauss–Newton method for atmospheric remote sensing. *Computer Physics Communications* 2002; **148**:214–226.
14. Carr JC, Beatson RK, Cherrie JB, Mitchell TJ, Fright WR, McCallum BC. Reconstruction and representation of 3D objects with radial basis functions. *ACM SIGGRAPH 2001*, Los Angeles, CA, 2001; 67–76.
15. Carr JC, Fright TJ, Batson RK. Surface interpolation with radial basis functions for medical imaging. *IEEE Transactions on Medical Imaging* 1997; **20**(Y):1–18.
16. Perrin F, Bertrand O, Pernier J. Scalp current density mapping: value and estimation from potential data. *IEEE Transactions on Biomedical Engineering* 1987; **BME-34**(4):283–288.
17. Franke R. Scattered data interpolation tests of some methods. *Mathematics of Computation* 1982; **38**(157): 181–200.
18. Kansa EJ. Multiquadrics—a scattered data approximation scheme with applications to computational fluid-dynamics—II. Surface approximations and partial derivative estimates. *Computers and Mathematics with Applications* 1990; **19**(8/9):147–161.
19. Kansa EJ. Multiquadrics—a scattered data approximation scheme with applications to computational fluid-dynamics—I. Solutions to parabolic, hyperbolic and elliptic partial differential equations. *Computers and Mathematics with Applications* 1990; **19**(8/9):127–145.
20. Turk G, O'Brien JF. Variational implicit surfaces. *Technical Report GIT-GVU-99-15*, Georgia Institute of Technology, 1999.

Copyright © 2005 John Wiley & Sons, Ltd.

21. Belytschko T, Parimi C, Moes N, Sukumar N, Usui S. Structured extended finite element method for solids defined by implicit surfaces. *International Journal for Numerical Methods in Engineering* 2003; **56**: 609–635.
22. Torrkulla J, Saxén H. Model of the state of the blast furnace hearth. *ISIJ International* 2000; **40**(5): 438–447.
23. Sorli K, Skaar IM. Monitoring the wear-line of a melting furnace. *3rd International Conference on Inverse Problems in Engineering 1999*, Port Ludlow, WA, 1999.
24. Schulte M, Klima R, Ringel D, Voss M. Improved wear-control at the blast furnace hearth by direct heat-flux measurements. *Ironmaking Conference Proceedings*, 1998; 607–614.
25. Kurpisz K. A method for determining steady state temperature distribution within blast furnace hearth lining by measuring temperature at selected points. *Transactions ISIJ* 1988; **28**:926–929.
26. Gonzalez M, Goldschmit MB, Zubimendi JL, Gonzalez N, Ametrano R, Giandomenico F. Inverse geometry problem of estimating the location of the 1150°C isotherm in a blast furnace hearth. *Proceedings of the 4th IAS Ironmaking Conference 2003*, San Nicolás, Argentina, 2003; 381–386.
27. Bathe KJ. *Finite Element Procedures*. Prentice-Hall: Englewood Cliffs, NJ, 1996.
28. Zienkiewicz OC, Taylor RL. *The Finite Element Method* (5th edn). Butterworth-Heinemann: Stonehamm, MA, 2000.
29. Appel JR, Gunzburger MD. Sensitivity calculation in flows with discontinuities. *Proceedings of the 14th AIAA Applied Aerodynamics Conference*, New Orleans, U.S.A., 1996; *Paper 96-2471*.
30. Brezinski C, Redivo-Zaglia M, Rodriguez G, Seatzu S. Multi-parameter regularization techniques for ill-conditioned linear systems. *Numerische Mathematik* 2003; **94**:203–228.
31. Luenberger DG. *Linear and Nonlinear Programming*. Addison Wesley: Reading, MA, 1984.

Copyright © 2005 John Wiley & Sons, Ltd.